Hindawi
Mathematical Problems in Engineering
Volume 2019, Article ID 8034619, 10 pages
https://doi.org/10.1155/2019/8034619

Research Article

Numerical Simulation on the Cavitation Flow of High Speed Oblique Water Entry of Revolution Body

Qing Mu, Yipin Lv, Kangjian Wang, Tianhong Xiong, and Wenjun Yi

National Key Laboratory of Transient Physics, Nanjing University of Science and Technology, Nanjing 210094, China

Correspondence should be addressed to Yipin Lv; yipinlv623@126.com

Received 7 September 2018; Revised 30 November 2018; Accepted 31 December 2018; Published 17 January 2019

Academic Editor: Andrea L. Facci

To explore the effects of water entry angle on the cavitation flow field of high-speed revolution body, based on the finite volume method, VOF (Volume of Fluid) multiphase model, Schnerr-Sauer cavity model, SST k-ω turbulence model, and dynamic mesh method, numerical simulation for modeling the oblique water entry of revolution body at high speed is performed. The evolution laws of cavity shape, motion characteristics, and hydrodynamic characteristics of revolution body at different water entry angles are analyzed. The results show that the numerical calculation method can effectively simulate the change of cavity shape during the water entry of the revolution body. With the increase of water entry angle, the uplift of liquid level decreases in the positive direction of the open cavity and increases in the negative direction. The angle of water entry has little effect on the velocity of the revolution body. The larger the angle of water entry, the greater the peak pressure and the faster the pressure decay at the moment of water entry.

1. Introduction

When the hydrodynamic forces act on the surface of the vehicle entering water at high speed, a low pressure region is formed locally. The liquid medium will vaporize and produce cavitation once the pressure at the minimum pressure point drops to the saturated vapor pressure of the liquid [1]. Large density ratio and high gradient flow field parameters arise at the fluid interfaces of cavitation flow, which brings remarkable difficulty in solving the numerical problem [2]. With a lot of complex flow phenomena, such as turbulence, phase transition, and compressibility, the process of water entry has the characteristics of unsteady, strong instantaneous and high load, which will have a significant impact on the motion and structure of the vehicle [3].

The angle of water entry is an important factor affecting the cavitation characteristics of flow field. A small angle of water entry will cause the body to swoop or come out of the water, and it can not move underwater along the extended line similar to the air trajectory. Too large entry angle may cause the vehicle to reach its destination late. Therefore, choosing the right angle of water entry is an important prerequisite for ensuring the ideal performance of the vehicle. Especially, in recent years, with the development of underwater weapons and the application of water surface recovery of spacecraft and rocket engines, it is more urgent and important to master the influence of water entry angle on the flow field characteristics of the vehicle in the process of water entry.

Logvinovich proposed the classical independent expansion principle of cavitation cross-section based on potential flow theory in 1960s and described the formation and evolution process of water entry cavitation. Savchenko et al. [4] carried out supercavitation tests in gravity water tunnel with initial velocity of 50-150 m/s. The cavity shapes and resistance characteristics of cavitators with different shapes were studied. Sun et al. [5] used incompressible velocity potential theory which features completely nonlinear boundary conditions to simulate the inclined water entry of various kinds of oblique cones. Yves-Marie S [6] developed a theoretical method for numerical solution of water entry into three-dimensional objects based on Wagner theory. The comparison with experimental results showed that the method is accurate and reliable. Xiong et al. [7] analyzed

the effect of small angle of attack on the cavity shapes of high-speed underwater projectiles. The angle of attack significantly changed the symmetry of the cavitation, which may lead to premature collapse of the cavitation and destabilization of the vehicle. Song et al. [8] studied the development law of cavity shapes, motion characteristics, and hydrodynamic characteristics of water entry of revolution bodies with different head, shaped by experiment and numerical simulation. Shi and Hu et al. [9, 10] carried out experiments and numerical simulations on supercavitation flow characteristics of bluff bodies with different head shapes entering water at different velocities. The results showed that the closure type of cavitation is deep closure when the initial velocity is small and surface closure when the initial velocity is large. According to the existing literatures, the numerical simulation of cavitation and flow field characteristics is mainly simplified as a single-degree-of-freedom vertical water entry. In practice, almost all the water entry problems encountered are inclined to water at an angle with the free surface, and the vertical water entry is only a simplified special case. In this paper, the CFD software Ansys Fluent 18.2 is used to simulate the inclined water entry process of a revolution body with an initial velocity of 500 m/s at three angles of 30°, 45°, and 60°. The development law of cavity shape, motion characteristics, and hydrodynamic characteristics of the revolution body at different angles are obtained. The research results can provide theoretical reference for engineering practice.

2. Numerical Model and Calculation Method

2.1. Governing Equation. It is generally believed that the effect of fluid compressibility can be neglected when the initial velocity is less than 700 m/s [11]. The numerical calculation assumes that the fluid medium is incompressible and neglects the heat conduction effect produced by the fluid viscosity; that is, it does not solve the energy equation. In addition, the effect of the detachment shock generated by the supersonic motion of the vehicle in the air on the water area and the attitude of the vehicle is not considered. The VOF multiphase flow model regards multiphase fluid as a single fluid medium mixture. According to the solution of water, air, and vapor three-phase flow problems, the volume fraction of water, air, and vapor is represented by α_l, α_g, α_v respectively. In any area of the whole flow field, they can be expressed as

$$\alpha_l + \alpha_g + \alpha_v = 1 \tag{1}$$

The continuity equation of the mixture is as follows:

$$\frac{\partial \rho_m}{\partial t} + \nabla \left(\rho_m v_m\right) = 0 \tag{2}$$

where $\rho_m = \alpha_v \rho_v + \alpha_g \rho_g + \alpha_l \rho_l$ is density of mixture, ρ_v, ρ_g, and ρ_l are the density of vapor, air, and water, respectively. v_m is mixture velocity vector, which under isothermal and isokinetic model is as follows:

$$v_m = v_v = v_1 = v \tag{3}$$

The momentum conservation equation of the mixed phase is as follows:

$$\begin{aligned} &\frac{\partial}{\partial t}\left(\rho_m u_i\right) + \frac{\partial}{\partial x_i}\left(\rho_m u_i u_j\right) \\ &\quad = -\frac{\partial p}{\partial x_i} + \frac{\partial}{\partial x_i}\left[\left(\mu_m + \mu_t\right)\left(\frac{\partial u_i}{\partial x_j} + \frac{\partial u_j}{\partial x_i}\right)\right] \end{aligned} \tag{4}$$

where u_i and u_j are the velocity vectors, x_i and x_j are the displacement vectors, p is the pressure, μ_m is dynamic viscosity of mixed medium, and $\mu_t = \rho k^2 C_u / \varepsilon$ is turbulent dynamic viscosity. k is turbulent kinetic energy, ε is turbulent dissipation rate, and C_u =0.09 is model constant.

$$\rho_m = \left(1 - \alpha_g - \alpha_v\right)\rho_l + \alpha_g \rho_g + \alpha_v \rho_v \tag{5}$$

$$\mu_m = \left(1 - \alpha_g - \alpha_v\right)\mu_l + \alpha_g \mu_g + \alpha_v \mu_v \tag{6}$$

In this paper, the cavitation problem in flow is solved by using the Schnerr and Sauer cavitation model, which describes the transport equation of the volume fraction of vapor as follows:

$$\begin{aligned} \frac{\partial \alpha_v}{\partial t} + \frac{\partial}{\partial x_i}\left(\alpha_v u_i\right) &= F_{vap}\frac{2\alpha_{nuc}\left(1 - \alpha_v\right)\rho_v}{R_B}\sqrt{\frac{2}{3}\frac{p_v - p}{\rho_l}} \\ &\quad - F_{cond}\frac{3\alpha_v \rho_v}{R_B}\sqrt{\frac{2}{3}\frac{p - p_v}{\rho_l}} \end{aligned} \tag{7}$$

In (7), R_B=1×10^{-6}m is the radius of the gas nucleus in the Rayleigh equation, α_{nuc}=5×10^{-4} is the volume fraction of noncondensable gases, and the F_{vap}=50 and F_{cond}=0.001 are the empirical constants.

In this study, we used the *k-ω SST* turbulence model to solve the fluid control equation. Menter [12] developed the *k-ω SST* model to efficiently blend the accurate formulation of the *k-ε* model at the far field and the *k-ω* model in the near-wall region. In this model, the turbulence kinetic energy and specific dissipation rate, respectively, are given as follows:

$$\begin{aligned} \frac{\partial\left(\rho k\right)}{\partial t} + \frac{\partial\left(\rho u_i k\right)}{\partial x_i} &= \frac{\partial}{\partial x_i}\left[\left(\mu + \frac{\mu_t}{\sigma_k}\right)\right]\frac{\partial k}{\partial x_i} - \beta' \rho k \omega \\ &\quad + P_k{}' \end{aligned} \tag{8}$$

$$\begin{aligned} \frac{\partial\left(\rho\omega\right)}{\partial t} + \frac{\partial\left(\rho u_i \omega\right)}{\partial x_i} &= \frac{\partial}{\partial x_i}\left[\left(\mu + \frac{\mu_t}{\sigma_\omega}\right)\frac{\partial \omega}{\partial x_i}\right] - \beta \rho \omega^2 \\ &\quad + \alpha_3 \rho S^2 \\ &\quad + 2\left(1 - F_1\right)\rho\frac{1}{\omega \sigma_{\omega 2}}\frac{\partial k}{\partial x_i}\frac{\partial \omega}{\partial x_i} \end{aligned} \tag{9}$$

where $P_k{}' = \min(P_k, 10\beta'\rho k\omega)$, $F_1 = \tanh(\arg_1{}^4)$ is a blending function, with

$$P_k = \mu_t \frac{\partial u_i}{\partial x_j}\left(\frac{\partial u_i}{\partial x_j} + \frac{\partial u_j}{\partial x_i}\right) \tag{10}$$

$$\arg_1 = \min\left[\max\left(\frac{\sqrt{k}}{\beta'\omega y}, \frac{500\nu}{y^2\omega}\right), \frac{4\rho\sigma_{\omega 2}k}{\mathrm{CD}_{k\omega}y^2}\right] \tag{11}$$

where ν is kinematic viscosity and y is the distance to the next surface.

$$\mathrm{CD}_{k\omega} = \max\left(2\rho\sigma_{\omega 2}\frac{1}{\omega}\frac{\partial k}{\partial x_i}\frac{\partial \omega}{\partial x_i}, 10^{-20}\right) \tag{12}$$

The turbulent eddy viscosity is defined as

$$\nu_t = \frac{\mu_t}{\rho} = \frac{k}{\max(\omega, SF_2)} \tag{13}$$

where S denotes the invariant measure of the strain rate and F_2 is another blending function which can be expressed as

$$F_2 = \tanh\left\{\left[\max\left(\frac{2\sqrt{k}}{\beta'\omega y}, \frac{500\nu}{y^2\omega}\right)\right]^2\right\} \tag{14}$$

All constant values are obtained from corresponding constants of the k-ε and the k-ω model such as $\alpha_3 = \alpha_1 F_1 + \alpha_2(1 - F_1)$. The values of the constants are $\beta' = 0.09$, $\alpha_1 = 5/9$, $\alpha_2 = 0.44$, $\beta_1 = 3/40$, $\beta_2 = 0.0828$, $\sigma_{k1} = 0.85$, $\sigma_{k2} = 1$, $\sigma_{\omega 1} = 0.5$, $\sigma_{\omega 2} = 0.856$.

It combines the advantages of the k-ε and k-ω turbulence model and adds the eddy viscosity limit equation to appropriately describe the transmission of turbulent shear stress. It has an remarkable advantage in predicting the near-wall flow and swirl [12].

2.2. Computational Model. According to the experimental data in reference [13], the ratio of the diameter of cavitator to the diameter of the rear body is greater than 0.26. The physical model is a revolution body with a cylindrical body and a disk head, the full-length L is 65 mm, the front cone length l is 15 mm, the largest diameter D is 10 mm, and the head disk diameter d is 3 mm. The revolution body is made of the ordinary steel with a density of ρ=7.85g/cm3. The symmetry surface shape of the revolution body is shown as Figure 1.

2.3. The Computational Domain and Boundary Conditions. The computational domain is a cylinder whose symmetry plane is shown in Figure 2. According to the simulation results in reference [14], the radial size of the basin should be 46 times larger than the maximum diameter of the revolution body to avoid the wall effect. The computational domain diameter is 1000mm, and the height is 2300mm. The gas-water junction is located at 25mm below the origin of coordinates, where the air domain height is 500mm and the water domain height is 2000mm. In initial state, the angle between the axis of the revolution body and the X axis is α, and the origin of the coordinate is placed at the middle point

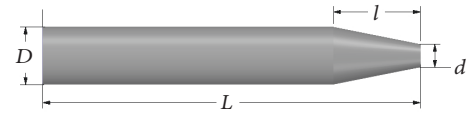

Figure 1: The shape of revolution body's symmetry plane.

of the head. The pressure exit boundary condition (pressure outlet) is used in the outer basin boundary, meanwhile the user defined function (UDF) is used for defining pressure on the boundary. The computational environment pressure P_0 is set to 101325Pa.

2.4. Dynamic Mesh Technique and Mesh Generation Method. The moving mesh model can be used for simulating the change of flow pattern with time caused by boundary movement. In this paper, the dynamic mesh technique is introduced to simulate the revolution body high-speed movement. Tetrahedral mesh is adopted, and the spring-based smoothing method and local remeshing method are used to update the mesh. By setting the size of the surface mesh of the model, and the range of size, when the mesh is compressed or pulled up beyond the set mesh size, it will merge or split the new grid layer.

Firstly, the mesh ideal height h_{ideal}, mesh splitting factor α_s, and mesh layer collapse factor α_c near the moving boundaries are specified, and then the mesh will be divided when the mesh height h_i satisfies (8) [15] during stretched period, or the compressed layer mesh is merged with its adjacent mesh into a new layer of mesh when the mesh height satisfies (9) during the compressed period.

$$h_i > (1 + \alpha_s)\, h_{ideal} \tag{15}$$

$$h_i < \alpha_c h_{ideal} \tag{16}$$

After introducing the dynamic mesh, it is equivalent to the pure convective motion of the mesh at a certain speed, and the convective effect of the mesh should be removed in practical calculation. Therefore, the unified form of conservation equation can be written as follows:

$$\frac{d}{dt}\int {}_V \rho_m \phi dV + \int {}_{\partial V} \rho_m \phi \left(u - u_g\right)\cdot dA = \int {}_{\partial V} \Gamma \nabla\phi \cdot dA + \int {}_V S_\phi dV \tag{17}$$

where ρ_m is the density of the fluid mixture, u is the velocity vector of the fluid, u_g is the velocity of the moving grid, Γ is the diffusion coefficient, $S\phi$ is the source term of the scalar ϕ, and ∂V represents the boundary of the control volume V.

In the present work, the cell is merged with the adjacent cell when the minimum length is less than 0.5 times that of the criterion, or the cell is split when the maximum length is larger than 0.5 times that of the criterion.

Using dynamic grid technology to solve unsteady problems often requires a lot of computing resources because of the computational analysis of the large volumes of data.

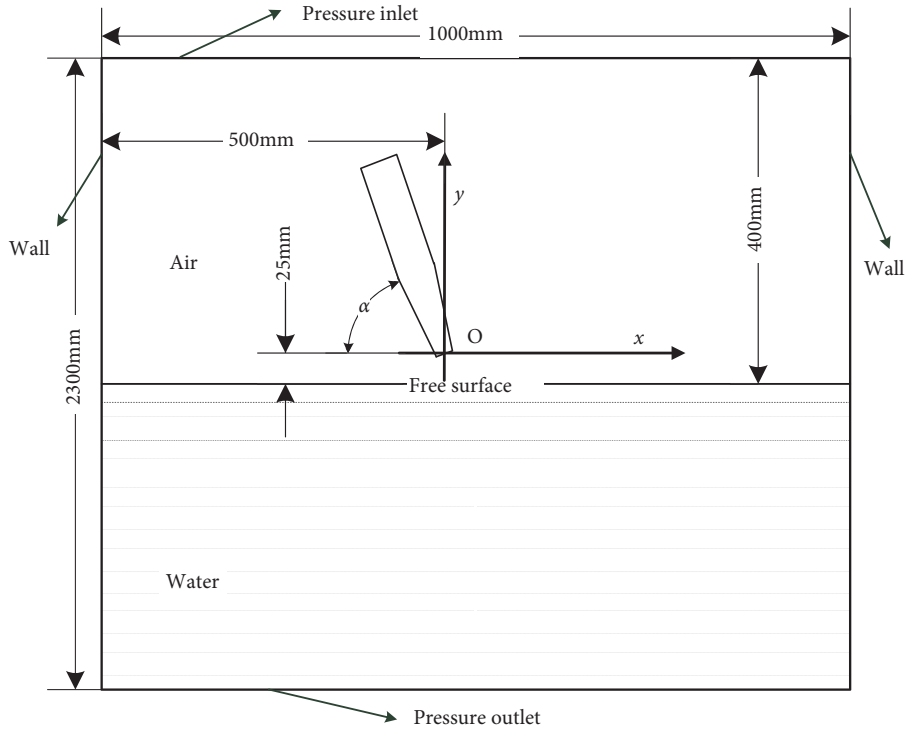

Figure 2: The schematic diagram of the computational domain.

Therefore, the computational domain is divided into the motion domain on the motion path of the revolution body and the static domain which is less affected by the motion of the revolution body for improving the calculation speed and precision. In order to improve the accuracy of the calculation result of air region, vapor-water interface and cavitation region, a more dense mesh is used in the motion domain and the mesh around the revolution body is further refined. The boundary layer mesh is defined near the wall of the revolution body. When we set up the dynamic mesh zones, the motion type of the revolution body and boundary layer mesh are set to rigid body, and other zones are set to stationary. In the present case, a total number of 1345,712 cells are adopted for the 3D mesh domain, the mesh in the motion domain and the static domain slip through a set of mesh interfaces, and in fluent, which are matched through the mesh interface tool. The mesh partition of computational domain is shown in Figure 3.

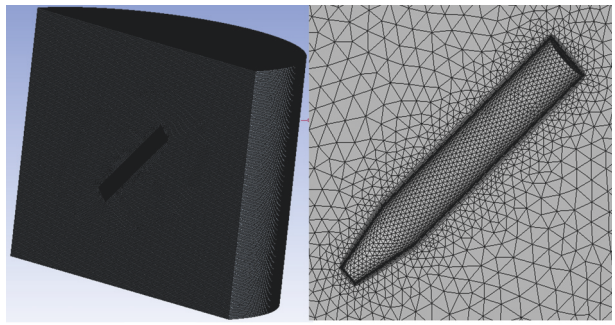

Figure 3: Sketch of the computational domain's mesh.

2.5. Numerical Method. In the process of water entry, the trajectory of a revolution body is determined by the inertia of the body itself and the forces (gravity, hydrodynamics, aerodynamics, etc.) and moments acting on the body. Therefore, the trajectory of revolution body is coupled with the calculation of the flow field. In this paper, firstly, the 6DOF solver provided by Ansys Fluent 18.2 is used to calculate the forces and moments acting on the revolution body surface during the water entry. Secondly, the translational acceleration is calculated according to the balance of forces (gravity, hydrodynamics, aerodynamics, etc.). Thirdly, the translational acceleration is calculated according to the balance of forces (gravity, hydrodynamics, aerodynamics, etc.), and then the translational velocity is obtained by integration. Meanwhile, the angular acceleration is calculated based on the balance of moments, and then the angular velocity is obtained by integration. Fourthly, the new position of the gravity center and new Euler angle are computed, and finally the oblique water entry trajectory of the revolution body is solved.

In this paper, the finite volume approach based on the VOF multiphase flow model is used to discrete the fluid governing equations. The pressure velocity coupling is solved using the Pressure Implicit with Split Operators (PISO) algorithm. The pressure field and velocity field were discretized using PRESTO and the second order upwind

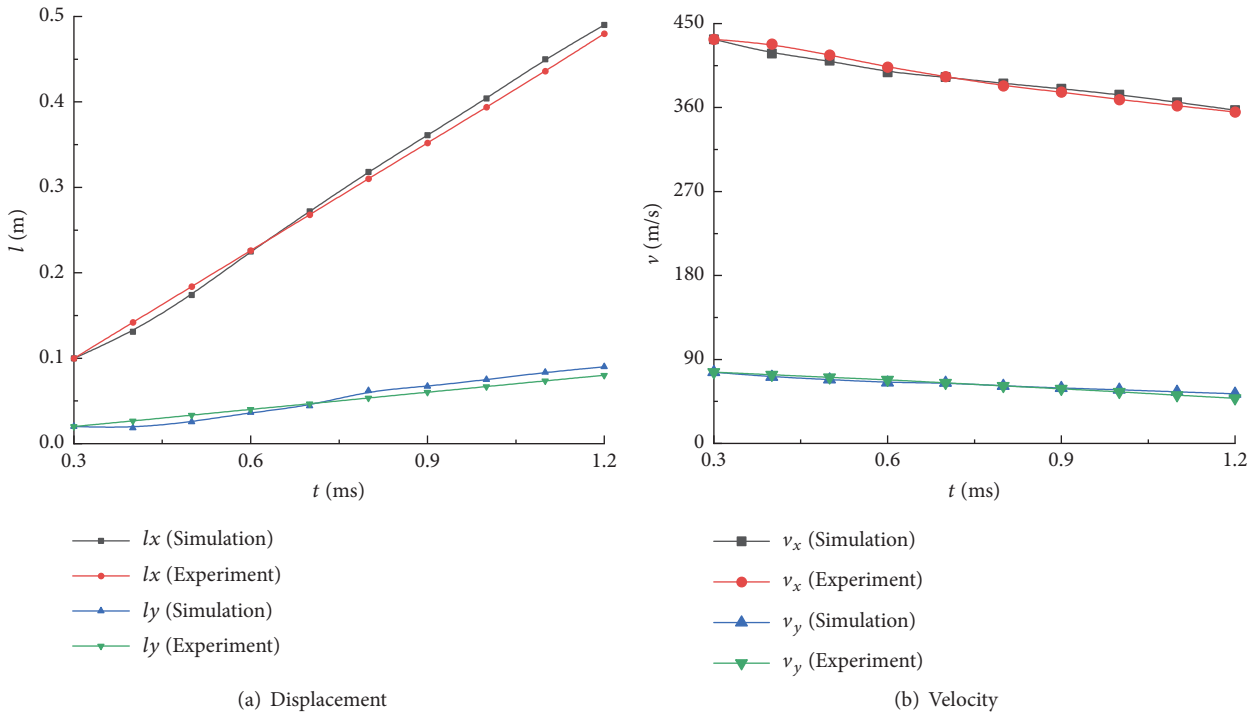

(a) Displacement (b) Velocity

Figure 4: Comparison of the change of displacement and velocity curves.

schemes, respectively, and the volume fractions of phases are discretized by using CICSAM. The user defined function (UDF) written in C is developed to define the mass of body, moment of inertia, and boundary pressure of computation domain and finally to achieve the water entry motion of revolution body.

2.6. Numerical Validation. At present, the study of high-speed water entry is still a relatively new study field in the world, and there are still many problems to be solved. (In this paper, the definition of high speed is that the initial velocity of water entry is 340m/s, which is higher than the sound speed in air.) Firstly, it is a great difficulty to conduct an experiment of high-speed water entry of vehicle. Secondly, the study object of high-speed water entry is mostly a small scale vehicle, and the water entry span is often only a few milliseconds. Besides, the cavitating flow field is a strong turbulence structure with the gas, vapor, liquid three-phase mixing, which has always been a difficult point in hydrodynamics experiments. Therefore, it brings overwhelming obstacles to get the pressure field and velocity field distribution of the flow field by experimental means. With the rapid development of computational fluid dynamics and improvement of computer performance in the late years, it becomes possible to calculate the cavitation flow field by numerical approach.

Based on the numerical simulation method proposed above, the incompressible liquid is adopted as the medium and the numerical simulation results are compared with the experimental results of the literature [16] to verify the rationality and confidence of the numerical model.

According to experimental details in Section 8.2 of the literature [16] the bullet was fired at 440m/s from the rifle barrel and entered the water tank at an angle of 10.7°. The length of the bullet is L=45 mm, and the head cavitator diameter is d=1.52 mm. The density of bullet is ρ=2.7g/cm3.

The numerical simulation of the experimental process is carried out according to experimental details of the literature [16], and the numerical calculation results are compared with the experimental results in paragragh 8.3.4 in terms of the displacement curve and the velocity curve.

In Figure 4, the numerical results of the curve and velocity variation of the high-speed revolution body are given. l_x and v_x represent the horizontal displacement and velocity of the high-speed revolution body, and the vertical displacement and velocity are represented by l_y and v_y, respectively. It can be seen from Figure 4 that the simulation results are in good agreement with experimental data of the literature [16]. It is also proved that the numerical simulation method used in the paper is correct and effective enough for modeling the oblipue water entry of revolution body.

3. Calculation Results and Analysis

The low pressure effect and water immersion resistance of revolution body are related not only to the head type and the ratio of length to diameter, but also to the initial angle of water entry. In this paper, the cavity shape, motion and hydrodynamic characteristics of the revolution body at different angles and different velocities are calculated by numerical calculation.

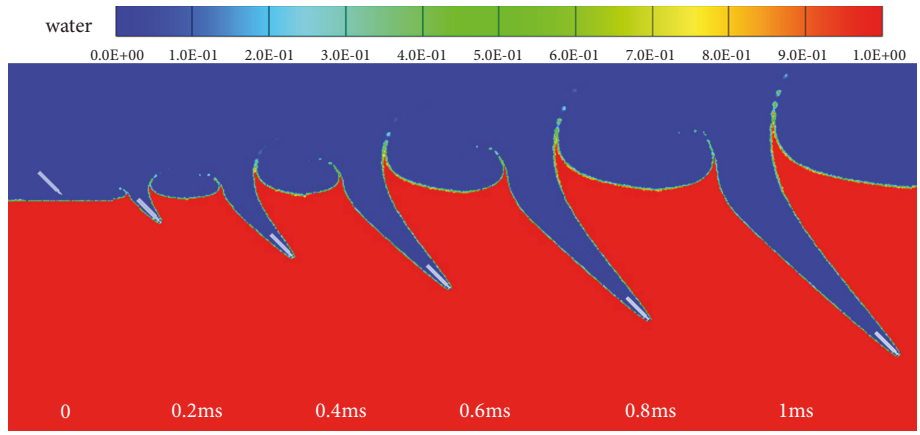

Figure 5: The cavitation morphology of 45° water entry.

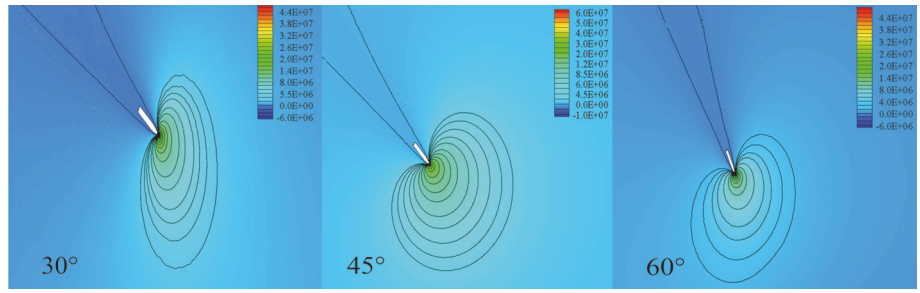

Figure 6: Pressure contours around the head of revolution body with different water entry angles at 0.5ms.

3.1. The Analysis of Cavity Shape and Flow Field. The water entry of revolution body at initial velocity of 500 m/s with angles of 30°, 45°, and 60° is numerically simulated, and the effects of different water entry angles on the cavity shape and hydrodynamic characteristics are analyzed.

Figure 5 shows the cavity change of revolution body entering water with an angle of 45°. It can be seen from Figure 5 that when the body tilts into the water, the lower side of the head touches the water firstly, causing splashing in front of the body. The raised pile of water around the rear part of revolution body is attached to the body, forming a low-pressure cavitation area between the water and revolution body because of the trapped air. At the same time, the hydrodynamic pressure is perpendicular to the wetting surface of the revolution body. Since the wetting surface is not a part of the sphere whose center coincides with the revolution body's center of gravity, the resultant force acting on the wetting surface of the revolution body will produce a moment around the revolution body's center of gravity, which makes the head of the revolution body deviates downward. After its head is completely immersed in water, the angle of attack becomes zero when the body continues to move forward and the pitching moment produced by hydrodynamic pressure becomes zero, and eventually the water entry angle of the body gradually is restored.

For an instant the revolution body enters the water, and the open cavity communicates with the atmosphere. After the maximum wetting area is reached at the head of the revolution body, the water begins to separate from the sharp part of the head, forming an inflatable cavity enclosing the front end of the head. As the body descends underwater, the volume of the cavity expands gradually, and the internal pressure drops below the atmospheric pressure, which makes the air in the atmosphere enter the cavity. From Figure 5, the revolution body enters the water to form an open cavity, which keeps expanding because of the entrainment of air from the water interface. Moreover, due to the high speed of water entry, the energy transferred to the water is enormous, and the cavity on the surface of the revolution body is not easy to be closed.

Figure 6 shows that the pressure distribution trends are basically consistent when the revolution body enters water with three different angles, and the maximum pressure is concentrated in the head of the revolution body.

Figure 7 shows the comparison of cavity shapes at different water entry angles at 0.5ms. It can be seen that due to the asymmetry of the head of the revolution body impacting the water surface during the inclined entering, a large part of the splashing occurs in the positive direction of the horizontal velocity component of the revolution body. Moreover, with the increase of water entry angle, the uplift of liquid level in the positive direction of the open cavity decreases, while that increases in the negative direction. This is because when the water entry angle is larger, the velocity component in the horizontal direction is smaller and the kinetic energy transmitted to the liquid in the positive direction of the

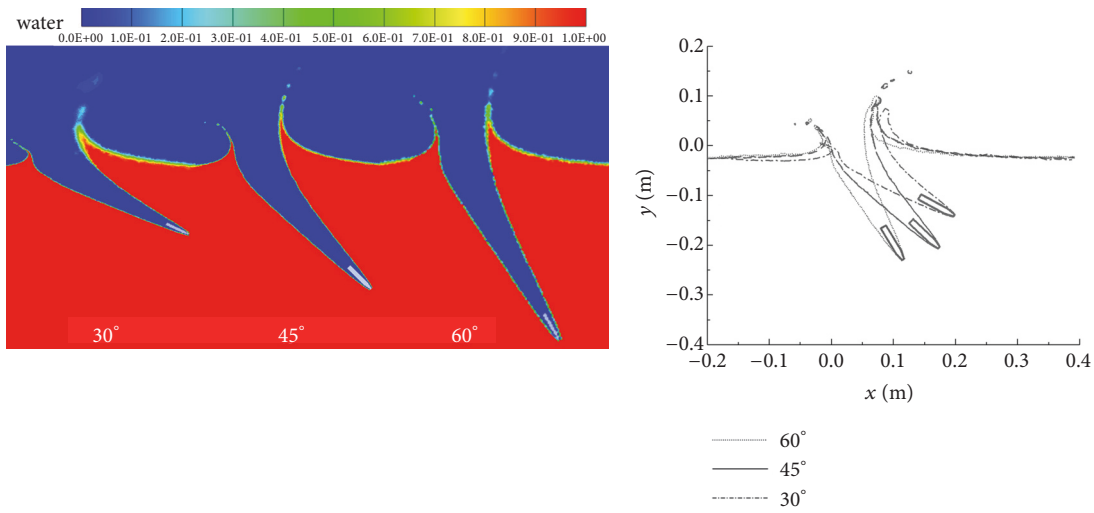

(a) Cavitation contours (b) Cavity shapes

FIGURE 7: Cavitation with different water entry angles at 0.5ms.

horizontal is smaller, so the uplift of the liquid level is smaller. While the velocity component in the vertical direction is larger, the kinetic energy transmitted to the liquid is larger, resulting in that the uplift of the liquid level in the negative direction is larger.

Figure 8 shows the volume fraction variation of gas and vapor phases during water entry at different angles. Due to the different angles of water entry, the cavitys produced by the revolution body in the process of water entry have marked difference. At the initial stage of water entry, the cavitys produced by the revolution body are slightly different at the free surface, and the cavitation contours are very similar. With the depth underwater increases, the difference of the cavity shape at the free surface becomes apparent. At the same time, the distributions of gas phase and vapor phase around the head of body fairly differ, which causes the difference in the pressure variation, eventually showing the significant difference in resistance characteristics of the revolution body.

3.2. Influence of Water Entry Angle on Motion Characteristics and Hydrodynamic Characteristics. In order to further explore the motion characteristics and hydrodynamic characteristics of revolution body with initial velocity of 500m/s tilting into water at three angles of 30°, 45°, and 60°, a numerical simulation of the water entry of a high-speed revolution body is carried out. The results are shown in Figures 9, 10, and 11.

Figure 9(a) shows that when the angle of water entry is 60°, the velocity decay in the 2ms time is greater than that of the other two cases due to that the wetting area of revolution body is larger when the water entry angle is larger. Meanwhile, the resistance and the kinetic energy loss are larger. In Figure 9(b), because of the difference in the initial direction of movement, the horizontal velocity decay rate of revolution body at the 30° angle of entry is larger than that of the 60°, and the vertical direction is the opposite. Generally speaking, the water entry angle has little effect on the total velocity. The slope of velocity decay curve is gradually decreasing, which indicates that the resistance of the revolution body reaches the maximum at the moment of water impact and then decreases gradually. The velocity decay of the revolution body with different water entry angles shows a nonlinear trend. With the increase of the water entry angle, the velocity decay rate of the revolution body increases.

Figure 10 shows the horizontal displacement lx and vertical displacement ly of the revolution body with different water entry angles. It can be seen that the displacement of the revolution body in horizontal and vertical direction in the 2ms time is about 55D, which indicates that there is a great resistance at the moment of water impact. At the same time, the smaller the water entry angle, the greater the horizontal displacement and the smaller the depth of water entry.

Figure 11 shows a comparison of the pressure variation curves of the revolution body with different water entry angles. It is shown that the pressure is nearly zero before reaching the water. The pressure has a peak at the moment when the body hits the free surface, and the pressure of the body can reach a thousand times the magnitude of the atmospheric pressure. The peak value of the pressure increases with the increase of the water entry angle. After the body touches water, with the increase of the depth underwater, the pressure decreases gradually and tends to be stable. The pressure gap between the revolution body with different water entry angles is getting smaller and smaller but still maintains a high level in the 2ms time. It can be seen that the revolution body will be affected continuously by the greater impact load in the early stage of high-speed water entry, which puts forward higher requirement for designing the structure of the water entry vehicle.

4. Conclusion

In this paper, a numerical simulation study on the oblique water entry of a truncated cone-nosed revolution body at

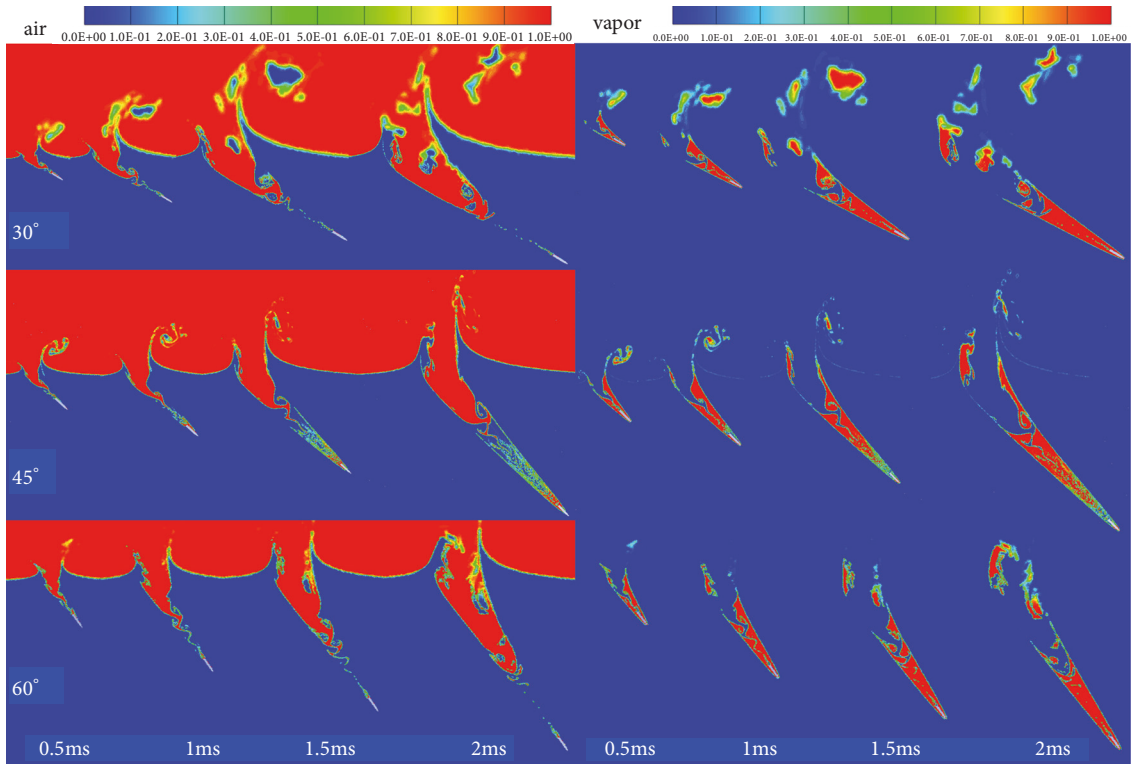

FIGURE 8: Variation process of volume fraction of air and vapor phase during revolution bodies' water entry.

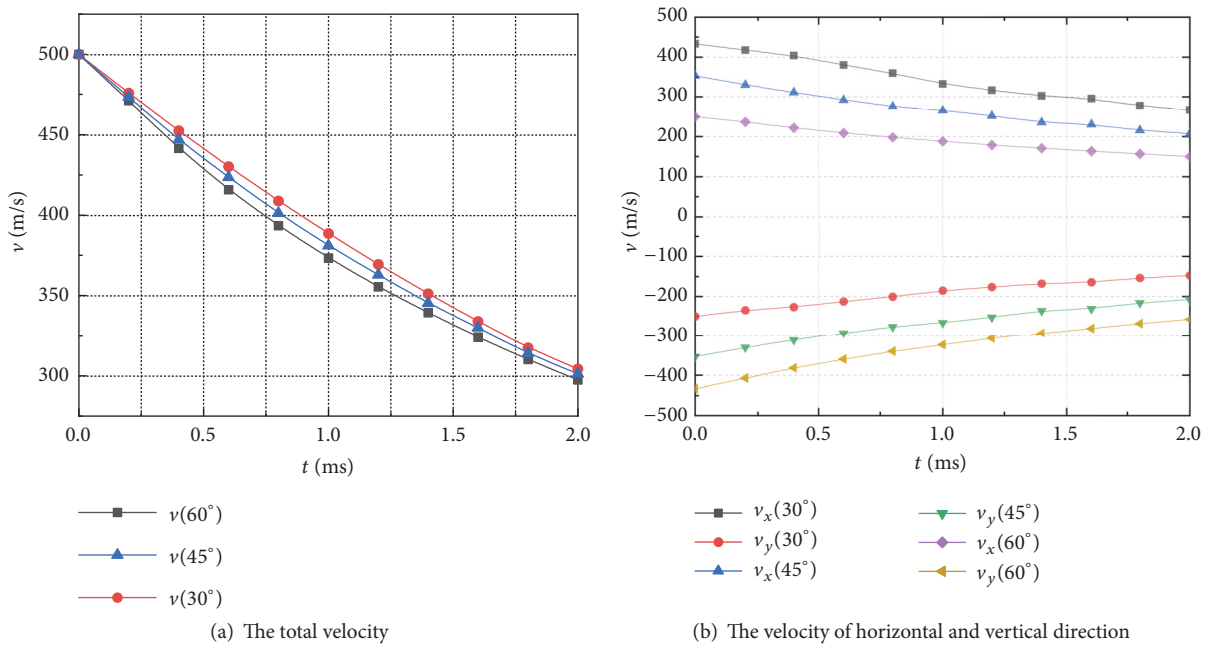

(a) The total velocity

(b) The velocity of horizontal and vertical direction

FIGURE 9: Velocity attenuation curves.

an initial velocity of 500 m/s with different angels is carried out. The cavity shape, hydrodynamic characteristics, and the motion characteristics of the revolution body are analyzed.

(1) The numerical calculation method adopted in this paper can effectively simulate the variation of cavity shape in the process of water entry. The cavity shape produced by the revolution body entering water at different angles are significantly different. With the increase of water entry angle, the uplift of liquid level decreases in the positive direction of the open cavity and increases in the negative direction.

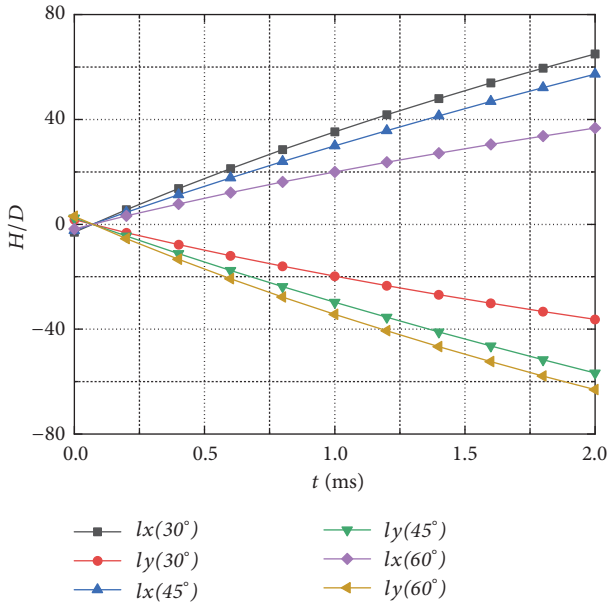

Figure 10: Displacement variation curves.

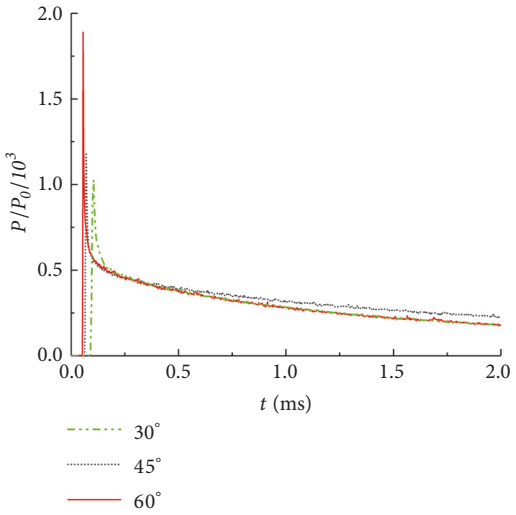

Figure 11: Comparison of pressure variation curves of revolution body.

(2) The velocity attenuation curves of revolution body with different water entry angles differ. With the increase of water entry angle, the attenuation rate of total velocity increases slightly. Generally speaking, the water entry angle has little effect on the total velocity variation of the revolution body.

(3) At the initial stage of water entry, the revolution body is subjected to a higher impact load, and the pressure peak can reach thousands of times of atmospheric pressure. The greater the water entry angle, the greater the pressure peak and the faster the pressure decay.

Data Availability

The datasets generated during the current study are not publicly available due to the data privacy policy of my research foundation but are available from the corresponding author upon reasonable request.

Conflicts of Interest

The authors declare that they have no conflicts of interest.

Acknowledgments

This work was supported by the National Natural Science Foundation of China (Grant nos. 11472136) and National Key Laboratory of Transition Physics Foundation (Grant nos. 61426040402 and 61426040403162604005).

References

[1] W. J. Yi and T. H. Xiong, "Research on drag characteristics of natural supercavitation profile for high speed bodies," *Ship Science & Technology*, vol. 31, no. 1, pp. 38–42, 2009.

[2] V.-T. Nguyen, D.-T. Vu, W.-G. Park, and C.-M. Jung, "Navier–stokes solver for water entry bodies with moving chimera grid method in 6DOF motions," *Computers & Fluids*, vol. 140, pp. 19–38, 2016.

[3] Q. P. Ma, *Investigation of multiphase flow characteristics induced by water entry of high speed projectiles*, Harbin Institute of Technology, 2014.

[4] Y. N. Savchenko, *Control of supercavitation Flow and stability of supercavitating motion of bodies*, Vki Lecture Series Supercavitating Flows, 2001.

[5] S. L. Sun and G. X. Wu, "Oblique water entry of a cone by a fully three-dimensional nonlinear method," *Journal of Fluids and Structures*, vol. 42, no. 4, pp. 313–332, 2013.

[6] S. Yves-Marie, "Oblique water entry of a three dimensional body," *International Journal of Naval Architecture and Ocean Engineering*, vol. 6, no. 4, pp. 1197–1208, 2014.

[7] T.-H. Xiong, W.-J. Yi, J.-J. Wu, and Y.-X. Liu, "Investigation on characteristic of supercaviting flow around underwater high speed vehicle at small angle of attack," *Ship Science & Technology*, vol. 31, no. 5, pp. 27–30, 2009.

[8] W. CH. Song, *Study on flow field characteristics of small-scale revolution body during water entry*, Harbin Institute of Technology, 2015.

[9] Q. Q. Hu, *Experimental observation and numerical calculation of supercavity flow of blunt body under different inclination angle into the water*, Zhejiang Sci-Tech University, 2014.

[10] H. H. Shi, Q. Q. Hu, B. Chen, and H. X. Jia, "Experimental study of supercavitating flows induced by oblique and vertical water entry of blunt bodies," *Explosion and Shock Waves*, vol. 35, no. 5, pp. 617–624, 2015.

[11] M. Lee, R. G. Longoria, and D. E. Wilson, "Cavity dynamics in high-speed water entry," *Physics of Fluids*, vol. 9, no. 3, pp. 540–550, 1997.

[12] F. R. Menter, M. Kuntz, and R. Langtry, "Ten years of industrial experience with the SST turbulence model," *Turbulence Heat & Mass Transfer*, vol. 4, pp. 625–632, 2003.

[13] L. P. Jia, *Numerical simulation and experimental study on supercavity characteristic induced by cavitators*, Harbin Institute of Technology, 2007.

[14] C. Huang, K. Luo, J. Dang, and D. Li, "Influence of flow field's radial dimension on natural supercavity," *Journal of Northwestern Polytechnical University*, vol. 33, no. 6, pp. 936–941, 1997.

[15] H.-T. Sui, P.-F. Li, S.-H. Ma, F.-Y. Ma, and Y. Hu, *Proficient in CFD dynamic grid engineering simulation and case practice*, People's Post and Telecommunications Publishing House, Beijing, China, 2013.

[16] T. T. Truscott, *Cavity dynamics of water entry for spheres and ballistic projectiles*, Massachusetts Institute of Technology, 2009.